Draft version December 4, 2018
Preprint typeset using LaTeX style emulateapj v. 12/16/11

LOW STAR FORMATION EFFICIENCY IN TYPICAL GALAXIES AT $Z = 5$–6

Riccardo Pavesi[1†], Dominik A. Riechers[1], Andreas L. Faisst[2], Gordon J. Stacey[1], Peter L. Capak[2]
[1]Department of Astronomy, Cornell University, Space Sciences Building, Ithaca, NY 14853, USA [2]Infrared Processing and Analysis Center, California Institute of Technology, Pasadena, CA 91125, USA

Draft version December 4, 2018

ABSTRACT

We report the detection of CO(2–1) line emission from a Lyman Break Galaxy at $z \sim 5.7$ with the VLA. The CO line luminosity implies a massive molecular gas reservoir of $(1.3 \pm 0.3)(\alpha_{\rm CO}/4.5\,M_\odot$ (K km s^{-1} pc^2)$^{-1}) \times 10^{11}\,M_\odot$, suggesting low star formation efficiency, with a gas depletion timescale of order ∼1 Gyr. This efficiency is much lower than traditionally observed in $z \gtrsim 5$ starbursts, indicating that star forming conditions in Main Sequence galaxies at $z \sim 6$ may be comparable to those of normal galaxies probed up to $z \sim 3$ to-date, but with rising gas fractions across the entire redshift range. We also obtain a deep CO upper limit for a Main Sequence galaxy at $z \sim 5.3$ with ~ 3 times lower SFR, perhaps implying a high $\alpha_{\rm CO}$ conversion factor, as typically found in low metallicity galaxies. Using ALMA, we find faint [NII] 205 μm emission relative to [CII] in all but the most IR-luminous "normal" galaxies at $z = 5 - 6$ for a sample including both CO targets, suggesting more intense or harder radiation fields in the ionized gas relative to lower redshift. These radiation properties indicate low metallicity may be common in typical $\sim 10^{10}\,M_\odot$ galaxies at $z = 5 - 6$, consistent with our CO measurements. Our sample shows evidence for high dust temperatures, and a young starburst producing high radiation intensity and hardness even with substantial dust obscuration. While a fraction of Main Sequence star formation in the first billion years may take place in conditions not dissimilar to lower redshift, lower metallicity may affect the remainder of the population.

1. INTRODUCTION

Massive galaxies started forming during the epoch of reionization at $z > 6$ and may have experienced their fastest growth toward the end of the first billion years of cosmic time ($z \sim 4 - 6$), doubling their stellar mass content on time-scales of order a hundred million years (e.g., Bouwens et al. 2015; Faisst et al. 2016). While the high redshift universe offers the promise of strong new constraints to dark matter physics through the early halo growth (e.g., Buckley & Peter 2017), they have, so far, been limited to coarse stellar mass-halo mass relationships which do not capture the variety in galaxy formation history hinted at by observations (e.g., Behroozi et al. 2018; Moster et al. 2018; Tacchella et al. 2018). The details of such an early growth epoch may also carry the imprint of re-ionization, therefore shining light on the physics of the dark ages (e.g., Ferrara 2016; Castellano et al. 2018; Ma et al. 2018).

Crucially, while abundant optical and near infrared (NIR) observations have revealed the end product of early galaxy formation (e.g., Bouwens et al. 2015), the drivers of such evolution are the gas processes of intense gas inflows, outflows, and cooling which lead to primordial star formation, galaxy growth, and dynamical assembly (e.g., Davé et al. 2011; Hopkins et al. 2014). Such gas flows are difficult to observe directly, but measurements of the gas conditions provide the most direct constraints on the physics of early galaxy evolution. For example, the observable gas phase metallicity probes the balance between gas inflows, outflows and metal enrichment due to star formation (e.g., Tremonti et al. 2004; Davé et al. 2012; Lilly et al. 2013). On the other hand, the relationship between local gas properties and star formation rate (the "star formation law") in early, forming galaxies provides the critical link between observable stellar properties and the more fundamental properties of the interstellar gas (e.g., Sharda et al. 2018; Krumholz et al. 2018). Since the "star formation law" may emerge from the complex effects of stellar feedback and local gas dynamics, it is of great interest to explore its redshift evolution and any variations across galaxy types and gas conditions (e.g., Daddi et al. 2010a; Genzel et al. 2015; Scoville et al. 2016, 2017; Tacconi et al. 2018; Orr et al. 2018).

The CO rotational transitions and the atomic fine structure lines in the far infrared (FIR) provide some of the most accurate tracers of the properties of the star-forming interstellar medium (ISM) in galaxies because they are bright, unaffected by dust extinction and probe all the main gas phases (e.g., Stacey et al. 1991; Hollenbach & Tielens 1997; Kaufman et al. 1999; Carilli & Walter 2013). In order to constrain the star formation law we need to trace the cold, molecular gas mass because it is found to be most causally connected to star formation in local galaxies (Schruba et al. 2011; Bigiel et al. 2011; Leroy et al. 2013; Carilli & Walter 2013). The best characterized tracers of such molecular gas are low-J rotational emission lines of the CO molecule, which have been calibrated within the Milky Way and in local galaxies, and achieve a high degree of consistency (e.g., Leroy et al. 2011; Sandstrom et al. 2013; Bolatto et al. 2013). These measurements may depend on metallicity estimates, since metallicity appears to strongly affect the fraction of molecular gas emitting CO lines and therefore, the gas mass-to-light ratio $\alpha_{\rm CO}$ (e.g., Maloney & Black 1988; Madden et al. 1997; Kaufman et al. 1999; Bolatto et al. 2013). However, it is difficult to measure metallicity directly in the cold molecular medium because no

†rp462@cornell.edu

hydrogen lines are directly accessible. Indirect tracers of metallicity typically involve either probes of the nitrogen abundance ratio to other metals or probes of the hardness and intensity of the radiation field (e.g., Masters et al. 2016; Vincenzo et al. 2016). The latter technique rests on observations of local dwarf galaxies, which have shown that lower metallicity environments may produce harder and more intense ultraviolet radiation, producing stronger lines from higher ionization states (e.g., Cormier et al. 2015).

Few observations of the ISM in galaxies at $z > 5$ are available, and the most luminous galaxies have preferentially been targeted to date, e.g., quasar hosts and the brightest dusty star forming galaxies (DSFGs, Maiolino et al. 2005, 2009; Walter et al. 2009, 2012; Riechers et al. 2013, 2014; Gullberg et al. 2015; Strandet et al. 2017). Although such brightness allows a great level of detail (e.g., Riechers et al. 2013), it is unlikely that the conditions in the most extreme outliers are representative of typical galaxies. For example, although the fraction of dust obscured star formation in extreme starbursts is close to unity, and the metallicity may be close to solar (e.g., Magdis et al. 2011), the first ALMA sample study of [CII] at 158μm and dust emission from normal galaxies at $z > 5$ found lower dust emission than expected from low redshift extrapolations (Riechers et al. 2014; Capak et al. 2015; Barišić et al. 2017; Faisst et al. 2017). The sample described by Capak et al. (2015) includes representative, massive galaxies ($M_* \sim 10^{10}\,M_\odot$) with optical spectra selected as Lyman Break Galaxies (LBGs) or Lyman Alpha Emitters (LAEs), two of the most common selection techniques at $z > 5$. While the ultraviolet luminosity and stellar mass of all sample galaxies is approximately equal, one of the main results of the ALMA observations was the wide range of [CII] and dust continuum luminosity observed. This wide range of FIR properties already in this small sample may suggest an evolutionary sequence, spanning the range from younger galaxies during their first major starburst to more "mature" and dust-rich galaxies bridging the gap to, traditionally sub-mm selected, DSFGs. This interpretation was confirmed by the analysis of the IRX/$\beta_{\rm UV}$ relation (Faisst et al. 2017), which found similar conditions as observed in massive galaxies at lower redshift in some while suggesting different dust properties (such as those observed in low metallicity dwarfs) for the others.

In order to constrain the conditions for star formation, low-J CO transitions provide the best probe and the most direct comparison to lower redshift surveys (e.g., Tacconi et al. 2013, 2018). The cold molecular gas properties in "normal" star-forming galaxies are poorly constrained beyond $z \sim 3$. Even at $z \sim 3-4$ few significant detections have been achieved, mostly afforded by strong gravitational lensing (Coppin et al. 2007; Riechers et al. 2010a; Dessauges-Zavadsky et al. 2015, 2017), a serendipitous detection at $z \sim 3.22$ (Gowardhan et al. 2017, Gowardhan et al. 2018, submitted), and constraining upper limits for unlensed targets (Tan et al. 2013). The low detection rate has suggested a strong evolution in $\alpha_{\rm CO}$ with redshift, possibly driven by a rapid metallicity evolution (Tan et al. 2013, 2014). However, as shown by Capak et al. (2015), standard selection techniques at $z > 5$ yield a wide range of dust obscuration, and suggest that a corresponding range of CO enrichment may also be present. We here present observations of the CO(2–1) transition from the FIR-brightest "normal" galaxy of the sample to obtain the first solid constraints at $z \sim 6$.

[CII] at 158μm is now commonly observed at high redshift due its high luminosity and it allows probing the gas dynamics in star-forming galaxies due to its widespread distribution (e.g., Stacey et al. 1991; Maiolino et al. 2005, 2009; Walter et al. 2009; Stacey et al. 2010; Riechers et al. 2013, 2014). The [CII]/IR luminosity ratio appears to trace the surface density of star formation, providing an important measure of starburstiness (e.g., Luhman et al. 1998; Malhotra et al. 2001). Furthermore, metallicity was shown to be the primary variable controlling the residual scatter in the [CII]/IR–$\Sigma_{\rm IR}$ relation (Smith et al. 2017). However, the [CII] line can originate from gas where hydrogen is ionized, neutral or molecular. Therefore observations of additional diagnostic lines that probe specific phases of the ISM are required to connect observations to physical conditions. In particular, the [NII] line at 205 μm is expected to be emitted under similar conditions of radiation intensity and gas density to [CII], but uniquely from the ionized phase (Oberst et al. 2006; Decarli et al. 2014; Pavesi et al. 2016; Díaz-Santos et al. 2017), therefore assessing the fraction of [CII] coming from the ionized rather than neutral gas. The [CII]/[NII] line ratio has been proposed as a metallicity tracer due to its sensitivity to abundance ratios (Nagao et al. 2011, 2012) and especially due to its sensitivity to the hardness of the radiation field (Pavesi et al. 2016) as traced by the ionization state of carbon and nitrogen in the ionized gas (Cormier et al. 2015). In the present work, we discuss inference from new ALMA measurements of the [NII] line luminosity in all the galaxies from the Capak et al. (2015) sample with dust continuum and [CII] detections.

In Section 2, we describe new spectroscopic observations of the CO(2–1) line transition from HZ10 (Capak et al. 2015), and we summarize analogous observations targeting LBG-1 (also named HZ6; Riechers et al. 2014; Capak et al. 2015) obtained as part of the CO Luminosity Density at High-z (COLDz) survey (Pavesi et al. 2018a). We also present new ALMA observations targeting the [NII] transition at 205 μm from the dust-detected sub-sample presented by Capak et al. (2015), composed of HZ4, LBG-1, HZ9 and HZ10, expanding our previous sample study (Pavesi et al. 2016). in Section 3 we present the results of the analysis of our CO and [NII] measurements. In Section 4 we discuss the implications of our measurements for the metallicity, the state of maturity of the star-forming ISM and the "star formation law" in this sample of "normal" galaxies at $z > 5$. Finally, we present our conclusions in Section 5. In this work, we adopt a Chabrier IMF and a flat, ΛCDM cosmology with $H_0 = 70\,{\rm km\ s^{-1}\ Mpc^{-1}}$ and $\Omega_{\rm M} = 0.3$.

2. OBSERVATIONS

2.1. *VLA observations of CO(2–1)*

We observed the CO(2–1) transition in HZ10 using NSF's Karl G. Jansky Very Large Array (VLA) in Ka band (project ID: 17A-011, PI: Pavesi). A complete description of these observations may be found in Pavesi et al. (2018b), which describes the properties of CRLE,

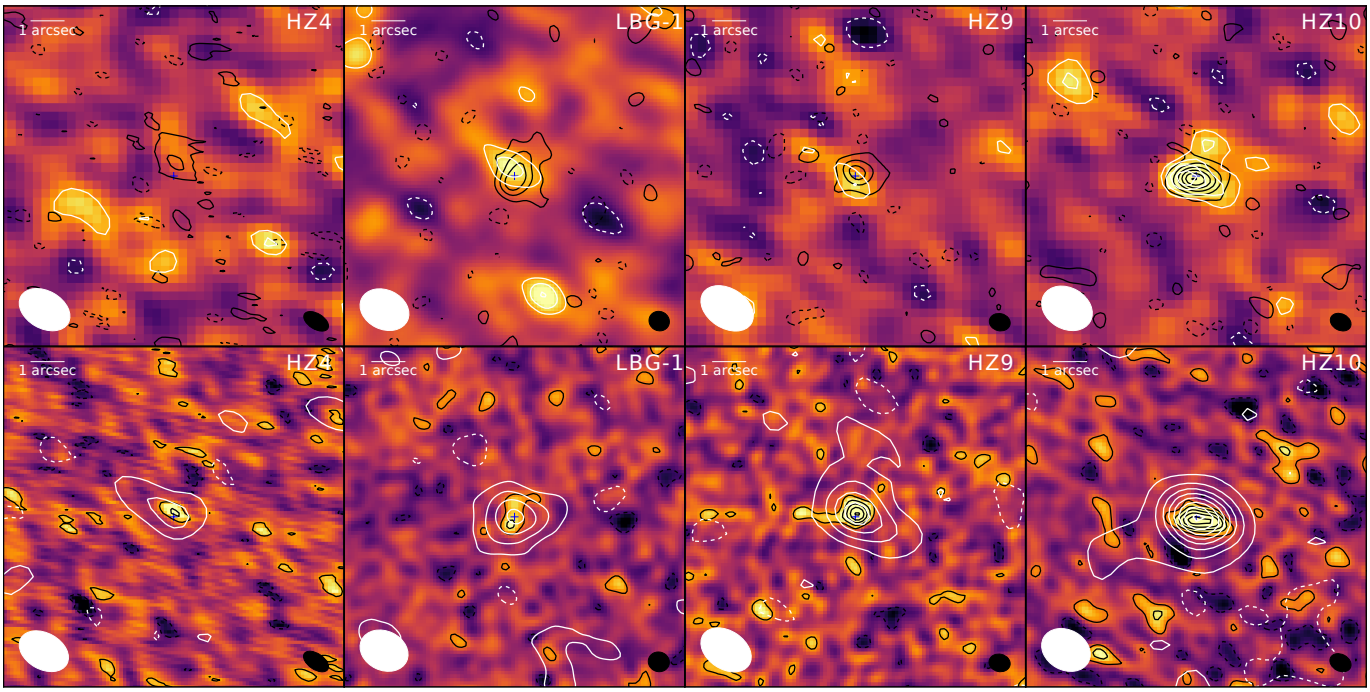

Figure 1. Top: Integrated line maps (over the line FWHM) showing [NII] color-scale with [NII] (white) and [CII] (black) contours overlaid. Blue crosses indicate the positions of the 205 μm continuum peak. The [NII] ([CII]) beam is shown in the bottom left (right) corner of each panel. The [NII] ([CII]) contours are multiples of 1σ (4σ), starting at $\pm 2\sigma$. The noise levels in the [CII] line maps are 0.07, 0.04, 0.11, 0.09 Jy km s^{-1} beam^{-1}, and in the [NII] line maps are 0.019, 0.016, 0.016, 0.04 Jy km s^{-1} beam^{-1}, respectively. Bottom: Continuum maps showing 158 μm color-scale with 205 μm (white) and 158 μm (black) contours overlaid. Contours start at $\pm 2\sigma$ and are in steps of 2σ (with the exception of the 205 μm contours in HZ9 and HZ10, in steps of 4σ). The 205 μm (158 μm) beam is shown in the bottom left (right) corner.

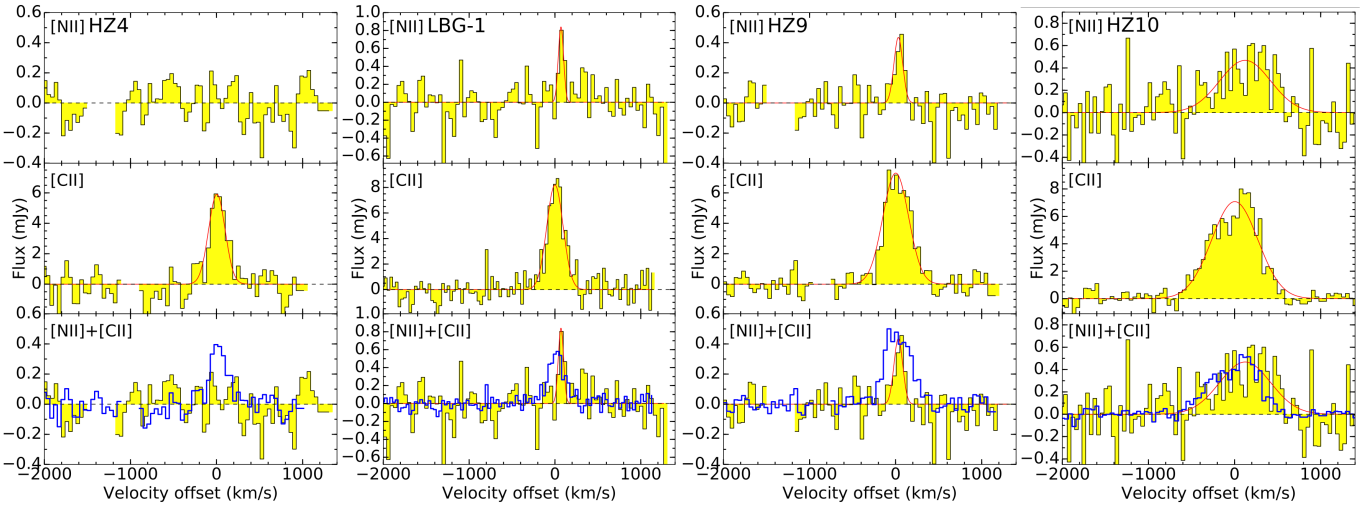

Figure 2. [CII] and [NII] spectra of our sample galaxies, and Gaussian fits to the line emission (red curves). The channel velocity width in all spectra is ~ 42 km s^{-1} (except in the LBG-1 [CII] spectra it is ~ 32 km s^{-1}). [CII] is scaled down by a factor 15 in flux density in the bottom panels for comparison (in blue).

an hyper-luminous DSFG at the same redshift as HZ10 and located within the same field view, with a separation of only 13″. In three of the eight observing sessions the two intermediate frequencies (IFs) were tuned to the central frequency of the CO(2–1) line in HZ10, and to the adjacent frequency range to maximize continuum sensitivity. However, in the remaining five sessions the second IF was moved in order to provide uninterrupted coverage of the CO(2–1) line in CRLE, by partially overlapping the first IF (Pavesi et al. 2018b). The total observing time was 19.8 hrs, on source. We image the data with the CLEAN algorithm in the Common Astronomy Software Application (CASA version 4.7, using natural weighting for maximal sensitivity. The imaging of the CO line data results in a synthesized beam size of $3.0'' \times 2.3''$ at the redshifted CO(2–1) frequency and $2.7'' \times 2.3''$ in the continuum map. The rms noise at the position of HZ10 (i.e., at the phase center) is $\sim 45\,\mu$Jy

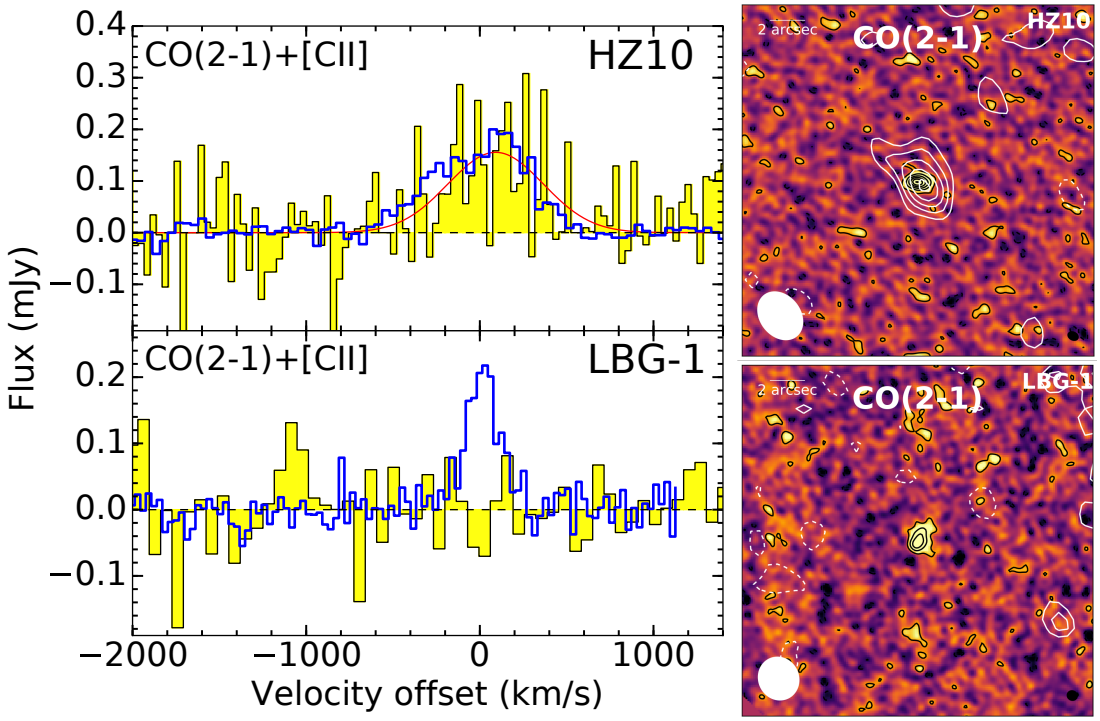

Figure 3. Left: CO(2–1) spectra of HZ10 and LBG-1, and Gaussian fit to the detected line emission (red curves). [CII] is shown scaled down by a factor 40 in flux density for comparison (in blue). The channel velocity width is ~ 40 km s^{-1} for HZ10 in both spectra, ~ 32 km s^{-1} and ~ 64 km s^{-1} for LBG-1 for [CII] and CO, respectively. Right: Integrated line maps (over the line FWHM) showing [CII] color-scale with CO(2–1) (white) and [CII] (black) contours. The CO(2–1) ([CII]) beam is shown in the bottom left (right) corner of each panel. The CO(2–1) ([CII]) contours are multiples of 1σ (4σ), starting at $\pm 2\sigma$. The noise levels in the [CII] line maps are 0.04, 0.09 Jy km s^{-1} beam^{-1} for LBG-1 and HZ10, respectively, and in the CO(2–1) line maps are 0.006, 0.010 Jy km s^{-1} beam^{-1} for LBG-1 and HZ10, respectively.

beam^{-1} in a 35 km s^{-1} wide channel. The final rms noise when averaging over the line-free 2.0 GHz of bandwidth is $\sim 2.7\,\mu$Jy beam^{-1}. The CO(2–1) transition in LBG-1 was observed as part of the COLDz survey (Pavesi et al. 2018a; Riechers et al. 2018) and a preliminary version was shown by Riechers et al. (2014). A complete description of these observations and of the imaging may be found in Pavesi et al. (2018a). The equivalent time on-source in the mosaic is 14 hours at the position of LBG-1. The imaging of the CO line data results in a synthesized beam size of $2.5'' \times 2.3''$ at the redshifted CO(2–1) frequency and $2.7'' \times 2.4''$ in the continuum map. The rms noise at the position of LBG-1 is $\sim 67\,\mu$Jy beam^{-1} in a 35 km s^{-1} wide channel. The final rms noise when averaging over the full 8 GHz of bandwidth is $\sim 1.3\,\mu$Jy beam^{-1}.

2.2. *ALMA observations of [CII] and [NII]*

Our observations of the [CII] line, data reduction and imaging for LBG-1 and HZ10 were previously described by Riechers et al. (2014); Capak et al. (2015); Pavesi et al. (2016). The ALMA Cycle-1 observations targeting the [CII] lines for HZ4 and HZ9, have previously been presented by Capak et al. (2015) and here we provide a brief description of the data that we have re-processed and re-analyzed. These observations were taken on 2013 November 4-16 in band 7 as part of a larger project (ID: 2012.1.00523.S, PI: Capak). The HZ4 pointing resulted in 20 min on source with 28 usable antennae. Ganymede was observed as flux calibrator, J0522−3627 was observed as bandpass calibrator, and J1008+0621 was observed as amplitude/phase gain calibrator. The HZ9 data resulted in 38 min on source with 27 antennae. Ganymede was observed as flux calibrator, J1037−2934 was observed as bandpass calibrator, and J1058+0133 was observed as amplitude/phase gain calibrator. In both cases the correlator was set up to target the expected frequency of the [CII] line and to provide continuous coverage of the continuum emission in adjacent spectral windows with channels of 15.6 MHz in Time Division Mode (TDM). The CASA version 4.5 was used for data reduction and analysis. All images and mosaics were produced with the CLEAN algorithm, using natural weighting for maximal sensitivity. For HZ4, the imaging results in a synthesized beam size of $0.8'' \times 0.5''$ at the redshifted [CII] frequency and in the continuum map. The rms noise in the phase center is ~ 0.5 mJy beam^{-1} in a 44 km s^{-1} wide channel and the final rms noise when averaging over all spectral windows (i.e. over a total 7.5 GHz of bandwidth) is $\sim 54\,\mu$Jy beam^{-1}. For HZ9, the imaging results in a synthesized beam size of $0.6'' \times 0.5''$ at the redshifted [CII] frequency and in the continuum map. The rms noise in the phase center is ~ 0.4 mJy beam^{-1} in a 43 km s^{-1} wide channel and the final rms noise when averaging over all spectral windows (i.e. over a total 7.5 GHz of bandwidth) is $\sim 47\,\mu$Jy beam^{-1}.

Cycle-3 observations of [NII] 205 μm targeting our sample galaxies were taken on 2016 January 1 and 5 in band 6, as part of two separate programs (2015.1.00928.S and 2015.1.00388.S, PIs: Pavesi and Lu, respectively) with one track from each program for HZ10 and LBG-1 and one track for HZ4 and HZ9 from the second program, taken in a compact configuration (max. baseline ~ 300 m). Observations from the first program were pre-

Table 1
Measured CO, [CII] and [NII] line properties of our sample galaxies

Quantity	HZ4	LBG-1	HZ9	HZ10
[CII] line properties				
$\nu_{\rm obs}$(GHz)	290.400 ± 0.013	301.980 ± 0.007	290.545 ± 0.019	285.612 ± 0.013
Redshift	5.5445 ± 0.0003	5.29359 ± 0.00015	5.5413 ± 0.0004	5.6543 ± 0.0003
$S_{\rm [CII]}$(mJy)	5.9 ± 0.7	8.2 ± 0.5	7.3 ± 0.9	7.1 ± 0.3
$FWHM_{\rm [CII]}$ (km s^{-1})	230 ± 30	230 ± 20	350 ± 50	630 ± 30
$I_{\rm [CII]}$ (Jy km s^{-1})	1.3 ± 0.3	2.1 ± 0.2	2.7 ± 0.3	4.5 ± 0.3
$L_{\rm [CII]}$ ($10^9 L_\odot$)	1.1 ± 0.3	1.71 ± 0.16	2.2 ± 0.2	4.0 ± 0.3
deconvolved size	$(1''.1 \pm 0''.3) \times (0''.6 \pm 0''.3)$	$(1''.00 \pm 0''.12) \times (0''.57 \pm 0''.10)$	$(0''.68 \pm 0''.12) \times (0''.48 \pm 0''.11)$	$(0''.80 \pm 0''.07) \times (0''.42 \pm 0''.06)$
size (kpc^2)	$(6.6 \pm 1.8) \times (3.6 \pm 1.8)$	$(6.2 \pm 0.7) \times (3.5 \pm 0.6)$	$(4.1 \pm 0.7) \times (2.9 \pm 0.7)$	$(4.8 \pm 0.4) \times (2.5 \pm 0.4)$
$S_{158\mu\rm m}$ (mJy)	0.24 ± 0.05	0.26 ± 0.07	0.60 ± 0.09	1.18 ± 0.16
[NII] line properties				
$\nu_{\rm obs}$(GHz)	—	232.114 ± 0.007	223.348 ± 0.009	219.49 ± 0.04
$S_{\rm [NII]}$ (mJy)	—	0.8 ± 0.2	0.4 ± 0.1	4.7 ± 0.8
$FWHM_{\rm [NII]}$ (km s^{-1})	—[a]	73 ± 19	120 ± 30	700 ± 130
$I_{\rm [NII]}$ (Jy km s^{-1})	< 0.06	0.06 ± 0.02	0.05 ± 0.02	0.34 ± 0.10
$L_{\rm [NII]}$ ($10^9 L_\odot$)	< 0.04	0.036 ± 0.012	0.032 ± 0.013	0.22 ± 0.07
$S_{205\mu\rm m}$ (mJy)	0.10 ± 0.02	0.20 ± 0.03	0.33 ± 0.04	0.83 ± 0.05
$L_{\rm [CII]}/L_{\rm [NII]}$	> 24	41^{+20}_{-10}	61^{+40}_{-17}	17^{+7}_{-4}
CO(2–1) line properties				
$\nu_{\rm obs}$(GHz)	—	—	—	33.157 ± 0.006
$S_{\rm CO}$ (mJy)	—	—	—	0.16 ± 0.03
$FWHM_{\rm CO}$ (km s^{-1})	—	—[a]	—	650 ± 140
$I_{\rm CO}$ (Jy km s^{-1})	—	< 0.018	—	0.10 ± 0.02
$L'_{\rm CO}$ (10^{10} K km s^{-1} pc^2)	—	< 0.44	—	2.9 ± 0.6
$S_{\rm 34GHz}$ (μJy)	—	< 4	—	< 7.8

Note. — All quoted uncertainties correspond to 1σ statistical uncertainty intervals and all limits correspond to 3σ. [a]: We assume FWHM equal to that of the [CII] line in order to derive upper limits on the line flux.

viously described in Pavesi et al. (2016), and the HZ10 observations for both programs were previously used in the analysis of CRLE in the field of view, presented by Pavesi et al. (2018b). We here present the remaining observations for LBG-1, HZ4 and HZ9. The two sets of observations for LBG-1 resulted in 64 min, and 18 min on source respectively, with ∼41–45 usable 12 m antennae under good weather conditions at 1.3 mm. The first set of observations was previously described by Pavesi et al. (2016). For the second set of observations of LBG-1, the nearby radio quasar J0948+0022 was observed regularly for amplitude and phase gain calibration, and J0854+2006 was observed for bandpass and flux calibration. The observations of HZ4 and HZ9 resulted in 30 and 47 min on source, with 45 and 47 usable 12 m antennae, respectively. The same radio quasar was observed for amplitude and phase calibration as for LBG-1, and J1058+0133 was observed for bandpass and flux calibration. The correlator was set up in identical configuration for these observations, to cover two spectral windows of 1.875 GHz bandwidth each at 15.6 MHz (~ 20 km s^{-1}) resolution (dual polarization) in Time Division Mode (TDM), in each sideband. We estimate the overall accuracy of the flux calibration to be within $\sim 10\%$. We used the Common Astronomy Software Application (CASA) version 4.5 for data reduction and analysis. We combined data from all observations, and produced all images with the CLEAN algorithm, using natural weighting for maximal point source sensitivity. Imaging the [NII] data for HZ4 results in a synthesized beam size of $1.6'' \times 1.1''$ at the redshifted [NII] frequency of HZ4 and in the continuum map. The rms noise in the phase center is ~ 0.14 mJy beam^{-1} in a 44 km s^{-1} wide channel. The final rms noise when averaging over the line free spectral windows (i.e. over a total 7.5 GHz of bandwidth) is $\sim 13\,\mu$Jy beam^{-1}. Imaging the [NII] data for LBG-1 results in a synthesized beam size of $1.5'' \times 1.2''$ at the redshifted [NII] frequency of LBG-1 and in the continuum map. The rms noise in the phase center is ~ 0.16 mJy beam^{-1} in a 40 km s^{-1} wide channel. The final rms noise when averaging over the line free spectral windows (i.e. over a total 7.5 GHz of bandwidth) is $\sim 15\,\mu$Jy beam^{-1}. Imaging the [NII] data for HZ9 results in a synthesized beam size of $1.7'' \times 1.2''$ at the redshifted [NII] frequency of HZ9 and in the continuum map. The rms noise in the phase center is ~ 0.15 mJy beam^{-1} in a 44 km s^{-1} wide channel. The final rms noise when averaging over the line free spectral windows (i.e. over a total 7.5 GHz of bandwidth) is $\sim 14\,\mu$Jy beam^{-1}. Imaging the [NII] data for HZ10 results in a synthesized beam size of $1.6'' \times 1.2''$ at the redshifted [NII] frequency of HZ10 and in the continuum map. The rms noise in the phase center is ~ 0.14 mJy beam^{-1} in a 44 km s^{-1} wide channel. The final rms noise when averaging over the line free spectral windows (i.e. over a total 7.5 GHz of bandwidth) is $\sim 19\,\mu$Jy beam^{-1} (Figures 1 & 2).

Table 2
Derived properties of our sample galaxies

Quantity	HZ4	LBG-1	HZ9	HZ10
$L_{\rm FIR}$ ($10^{11}\,L_\odot$)	$5.2^{+4.6}_{-2.6}$	$4.9^{+4.4}_{-2.6}$	12^{+10}_{-6}	13^{+11}_{-7}
SFR ($M_\odot$ yr^{-1})	52^{+46}_{-26}	49^{+44}_{-26}	120^{+100}_{-60}	130^{+110}_{-70}
M_* ($10^9\,M_\odot$)[a]	$4.7^{+2.9}_{-1.8}$	15^{+6}_{-5}	$7.2^{+5.0}_{-2.9}$	25^{+12}_{-8}
$M_{\rm gas}$ ($10^{10}\,M_\odot$)[b]	—	< 2	—	13 ± 3
$M_{\rm dyn}(< R_{1/2})$ ($10^{10}\,M_\odot$)	$1.8^{+1.3}_{-1.0}$	$1.9^{+0.6}_{-0.4}$	$3.5^{+3.1}_{-1.6}$	10 ± 3

Note. — All quoted uncertainties correspond to 1σ intervals and all limits correspond to 3σ. [a]: Stellar masses reported by Capak et al. (2015). [b]: Gas masses are derived from the CO luminosity assuming a Galactic $\alpha_{\rm CO} \sim 4.5$ conversion factor.

3. ANALYSIS

3.1. *Results from the dust continuum measurements*

We detect dust continuum emission from the full galaxy sample at 158 μm and 205 μm (Figure 1, Table 1). No continuum signal is detected in the VLA observations targeting HZ10 and LBG-1 at ∼34 GHz (corresponding

to rest-frame ~ 1.3 mm), yielding deep 3σ upper limits (Table 1). We measure the continuum flux at 158 μm and 205 μm by imaging all line-free channels using natural baseline weighting, and using the CASA task IMFIT to fit a 2D Gaussian model to the emission.

We fit these continuum fluxes with a modified blackbody smoothly connected to a mid-IR power law (Pavesi et al. 2016). We adopt high dust temperature priors, as suggested by Faisst et al. (2017) for these galaxies. We employ Gaussian priors for the dust emissivity β parameter (1.7 ± 0.5), for the dust temperature (60 ± 15 K), for the mid-IR power law index (2.0 ± 0.5) and for the transition rest-frame wavelength to the optically thick regime ($60\pm20\,\mu$m). We note that the relative fluxes at 158 μm and 205 μm across our sample suggest a diversity of dust SED shapes, hinting to possible lower dust temperatures in LBG-1 and HZ10 relative to the rest of the sample, which may be consistent with the higher stellar masses in these two galaxies. However, the available constraints are not sufficient to resolve the degeneracy between dust temperature and emissivity index variations. We derive Far-IR (FIR) luminosities by integrating between 42.5 and 122.5 μm (Table 2). Because the dust spectral energy distributions (SEDs) are not constrained in the mid-IR, we follow the standard practice of adopting the FIR luminosities as an estimate of total IR, without extrapolating to shorter IR wavelengths (e.g., Riechers et al. 2014; Pavesi et al. 2018b). We caution, however, that this is likely to be an under-estimate, and that the total IR luminosity may be $\sim$1.5-2$\times$ higher than the FIR.

We can use the available dynamical mass and Rayleigh-Jeans dust continuum emission estimates to provide constraints to the gas masses in these galaxies, independently from the CO measurements. Dust mass estimates based on the full SED fitting may be unreliable because they are strongly dependent on the model dust temperature distribution, which is poorly constrained for our sample galaxies. Alternatively, the Rayleigh-Jeans dust continuum emission may be used to estimate dust and gas masses, assuming an average emissivity and dust temperature for the dominant cold dust component, and a constant dust-to-gas ratio (Hildebrand 1983; Eales et al. 2012; Scoville 2013; Scoville et al. 2013, 2016, 2017; Bourne et al. 2013; Groves et al. 2015). The dependence on cold dust temperature and dust-to-gas ratio may make the Rayleigh-Jeans method less reliable than at lower redshifts (e.g., Pavesi et al. 2018b). On the other hand, the opposing effects of increasing dust temperatures, and decreasing dust-to-gas ratios that may occur in "normal" galaxies at high redshift may partially compensate each other. The 34 GHz upper limits imply 3σ gas mass limits of $< 2.8\times10^{11}\,M_\odot$ for HZ10 and $< 1.6\times10^{11}\,M_\odot$ for LBG-1, adopting the relation derived by Scoville et al. (2016, 2017). We also use the $\sim$230 GHz continuum fluxes to derive approximate estimates, although these measurements may not lie on the Rayleigh-Jeans tail, and therefore may not accurately trace the cold dust component. These continuum measurements would imply gas masses of $\sim 1.3\times10^{10}\,M_\odot$ for HZ4, $\sim 2.5\times10^{10}\,M_\odot$ for LBG-1, $\sim 4.4\times10^{10}\,M_\odot$ for HZ9, and $\sim 1.1\times10^{11}\,M_\odot$ for HZ10, with large systematic uncertainties.

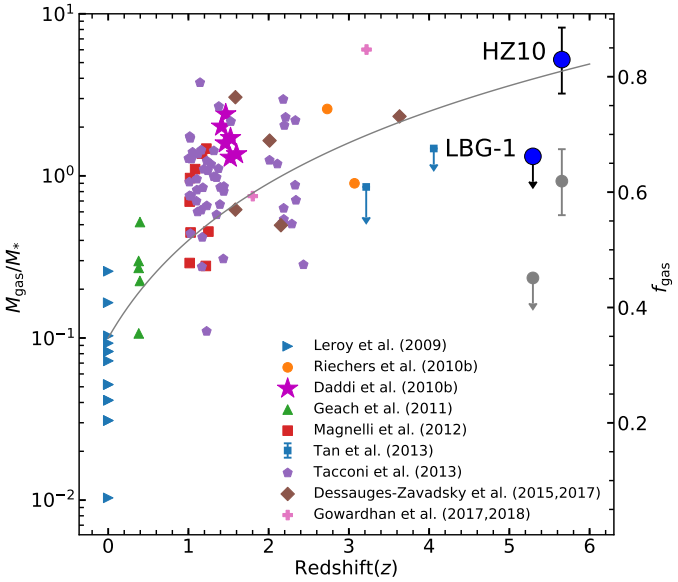

Figure 4. The ratio of molecular gas mass to stellar mass (calculated using an $\alpha_{\rm CO}$=4.5 $M_\odot\,({\rm K\,km\,s^{-1}\,pc^2})^{-1}$ for all sources) adapted from Carilli & Walter (2013); Leroy et al. (2009); Riechers et al. (2010a); Daddi et al. (2010b); Geach et al. (2011); Magnelli et al. (2012); Tan et al. (2013); Tacconi et al. (2013); Dessauges-Zavadsky et al. (2015, 2017); Gowardhan et al. (2017) The grey line shows $M_{\rm gas}/M_* \propto (1+z)^2$ (Geach et al. 2011). An alternative choice of $\alpha_{\rm CO}$=0.8 for HZ10 and LBG-1 is also shown in light grey.

3.2. *Results from the CO measurements*

We detect CO(2–1) line emission from HZ10 with a significance of $\gtrsim 8\sigma$, and provide a constraining upper limit to the CO(2–1) emission toward LBG-1 (Figure 3). We extract an aperture spectrum for HZ10[1] and a single pixel spectrum at the peak position of the [CII] emission toward LBG-1, in order to measure or constrain the CO(2–1) line properties (Table 1). The CO(2–1) emission toward HZ10 appears slightly resolved, although the coarse resolution of compact array configuration observations does not allow a precise size determination. We use CASA UVMODELFIT to fit a circular Gaussian model to the line visibilities in HZ10 and derive a deconvolved FWHM size of $1''.2\pm0''.4$ for the CO(2–1) emission, corresponding to 7 ± 2 kpc, which is compatible with the [CII] and [NII] size estimates.

While the CO(2–1) line luminosity is expected to provide a reliable estimate of the molecular gas mass, several factors affect the proportionality factor such as heating from, and contrast against, the cosmic microwave background (CMB; e.g., da Cunha et al. 2013) and the strong metallicity dependence of the CO luminosity per unit molecular gas mass (e.g., Bolatto et al. 2013). Here, we further assume a brightness temperature ratio of $R_{21}=1$ between the CO J=2–1 and 1–0 transitions.[2] Contrast against the warmer CMB, and the additional gas heating this provides at $z>5$ is only weakly constrained with-

[1] We adopt elliptical apertures of sizes equal to the FWHM of the best fit 2D Gaussian to the integrated line emission.

[2] Current samples of high redshift dusty star-forming galaxies, and main-sequence galaxies show nearly thermalized gas excitation up to the J=2–1 transition, justifying this assumption ($R_{21}\sim0.80-0.95$; e.g., Carilli & Walter 2013; Daddi et al. 2015).

out additional CO excitation measurements. da Cunha et al. (2013) suggest that we may expect the observed CO line flux to be suppressed by a factor $\sim 1.25 - 2$ at this redshift. We do not attempt to estimate this effect independently, but simply absorb it into the definition of $\alpha_{\rm CO}$.

Our constraints indicate that CO(2–1) line emission from LBG-1 is unexpectedly weak, relative to low redshift trends. This may be a consequence of low metallicity and relatively low dust abundance (Bolatto et al. 2013). LBG-1 shows an unusually high inferred [CII]/CO(1–0) luminosity ratio ($\gtrsim 9000$, Figure 3), relative to the value in HZ10 (~ 3000) and to the values commonly measured in local starbursts (~ 4400; e.g., Wolfire et al. 1989; Stacey et al. 1991, 2010) and high redshift dusty star forming galaxies (5200 ± 1800; e.g., Gullberg et al. 2015). The high ratios observed in LBG-1 are difficult to explain within standard PDR models, but naturally arise as a consequence of lower metallicity (e.g., Maloney & Black 1988; Stacey et al. 1991; Madden et al. 1997). In particular, low metallicity dwarfs typically show similar ratios of $\sim 7000 - 10^5$ (e.g., Cormier et al. 2014; Jameson et al. 2018). On the other hand, the ratio observed in HZ10 points to star-forming gas conditions which are typical of "normal" lower redshift Main Sequence galaxies.

We can use the gas mass estimates based on the Rayleigh-Jeans dust continuum emission to constrain the $\alpha_{\rm CO}$ conversion factor by assuming that the gas mass is dominated by molecular gas. The main uncertainties inherent in the Rayleigh-Jeans dust method are a dependence on the gas-to-dust ratio and on dust properties affecting the dust SED. These estimates would imply constraints to $\alpha_{\rm CO}$[3] of $\lesssim 10$ (~ 4 based on the 220 GHz flux) for HZ10 and $\gtrsim 5.7$[4] based on the 230 GHz flux for LBG-1. These are in agreement with our inference of "normal" star-forming conditions for HZ10 and of lower metallicity gas in LBG-1.

3.2.1. *Dynamical mass analysis and gas masses constraints*

We have carried out a dynamical modeling analysis directly on the visibilities for the [CII] observations in HZ9 and HZ10, following the method previously described by Pavesi et al. (2018b). We simultaneously fit a rotating disk model generated by KinMS (Davis et al. 2013) to the line emission and a simple continuum model (one and two Gaussian components for HZ9 and HZ10, respectively). While the [CII] line in HZ9 and HZ10 shows a smooth velocity gradient, the line in LBG-1 shows a more complex morphology and dynamics, with three components, and two separate velocity gradients (Riechers et al. 2014). Therefore we do not attempt modeling the emission from LBG-1, as the data are not sufficient to properly constrain such a high-complexity model. Although the [CII] line in HZ10 shows a smooth velocity gradient, the *HST* NIR and dust continuum images from ALMA suggest the presence of two separate morphological components. These may be associated with either a galaxy merger, or with clumpy gas and stellar distributions, embedded in a rotating disk. The somewhat asymmetric [CII] line profile may also be caused by massive gas clumps, as shown by the simulations of Daddi et al. (2010b); Bournaud et al. (2014, 2015). Because of the limitation of assuming a single disk model, we note that substantial uncertainties regarding the detailed dynamics of HZ10 affect our inference as evidenced by the non-negligible residual structure after model fitting (Appendix A).

We use the disk model scale-length and rotation curve to derive dynamical mass estimates within the half-light radius, by adopting the measured rotational velocity (Appendix A). We do not apply corrections for velocity dispersion because the physical origin of the apparent dispersion is uncertain (particularly in the case of HZ10, for which two distinct components may be partly responsible for the line broadening). We estimate that these systematic corrections may be as large as $\sim 50\%$, toward increasing the dynamical masses inferred by fitting a rotating disk, based on the measured gas dispersion ($\sigma \sim 90 \pm 10\,{\rm km\,s^{-1}}$ and $220 \pm 10\,{\rm km\,s^{-1}}$ for HZ9 and HZ10, respectively). We obtain $\sim (6.1 \pm 0.7) \times 10^{10}\,M_\odot$ for HZ10 and only an approximate estimate of $5^{+5}_{-3} \times 10^{10}\,M_\odot$ for HZ9, within the half light radius of the [CII] emission. Our results agree within the uncertainties with previous estimates based on tilted-ring modeling in the image plane by Jones et al. (2017), although our uncertainty estimates are significantly more conservative due to the larger number of fitted parameters. We also use the dynamical mass estimation method by Daddi et al. (2010b), which was calibrated on disk galaxy simulations, to derive dynamical mass estimates for our full sample, based on the measured [CII] size. We apply this technique by using the line FWHM, the fitted size of the [CII] emission and the disk inclination from the ratio of minor to major axes (the latter is compatible with our results from UV-space dynamical modeling). We derive dynamical masses within the half light radius for the full galaxy sample using the method by Daddi et al. (2010b) and list them in Table 2. These are in agreement with our previous gas estimates, within the large uncertainties of both methods utilized. The inferred dynamical mass for LBG-1 is ~ 2.5 times lower than previous estimates, although within the original uncertainties, due to a revised [CII] size and due to differences in the method employed (Riechers et al. 2014). However, dynamical mass estimates for LBG-1 may be affected by potential multiplicity. In the following, we adopt these dynamical mass estimates based on the Daddi et al. (2010b) method for HZ9 and HZ10 as well, because they are compatible with our estimates based on UV-space dynamical modeling, and because they are based on a simulation-based calibration that includes the expected turbulent pressure contribution to the inferred circular velocity.

We can use these dynamical masses to provide coarse estimates of the total gas mass, by accounting for the

[3] Units of $M_\odot\,({\rm K\,km\,s^{-1}\,pc^2})^{-1}$ assumed throughout the following

[4] In order to deal with relative uncertainties of order unity throughout this work, we adopt the convention of quoting Gaussian-equivalent percentiles. Therefore, uncertainty ranges correspond to 16th, 50th and 84th percentiles and 3σ limits are defined to imply a 99.7% probability. Propagation of these uncertainties to derived quantities was carried out by numerical sampling and evaluation of posterior distribution percentiles. Lognormal distributions were used to sample skewed distributions described by asymmetric 1σ ranges. Upper limits from non-detections are treated as positive-truncated (enforcing a uniform prior), 0-centered Gaussians with specified standard deviation as determined by the noise level.

contribution of stellar and dark matter masses (25%) according to Daddi et al. (2010b). These dynamical mass estimates would imply total gas masses of $(1.4 \pm 0.9) \times 10^{10}\,M_\odot$ for LBG-1, $4.5^{+4.5}_{-2.5} \times 10^{10}\,M_\odot$ for HZ9 and $(1.2 \pm 0.5) \times 10^{11}\,M_\odot$ for HZ10. If we assume this gas mass to be dominated by molecular gas, these estimates imply $\alpha_{\rm CO}$ (in units of $M_\odot\,(\mathrm{K\,km\,s^{-1}\,pc^2})^{-1}$) $4.2^{+2}_{-1.7}$ for HZ10, but do not provide a significant constraint for LBG-1[5]. The derived $\alpha_{\rm CO}$ factor for HZ10 is compatible with the Milky Way value (~ 4.5, in the same units) which may also apply to $z \sim 1-2$ main-sequence disk galaxies (Daddi et al. 2010b; Carilli & Walter 2013; Tacconi et al. 2013; Genzel et al. 2015). In the following, we assume a fixed value of $\alpha_{\rm CO} = 4.5$ for definiteness, in order to derive and constrain gas masses in HZ10 and LBG-1 (Table 2, Figure 4), with the caveat that this value may only be a lower limit in the case of LBG-1, due to metallicity effects.

3.2.2. *Constraints to high redshift star formation*

To study the star formation efficiency in HZ10 and LBG-1, first we directly compare the FIR to CO luminosity (Figure 5) relative to expectations based on previous determinations of the star formation law in the local and high redshift Universe (Carilli & Walter 2013). The Main Sequence star formation law by Daddi et al. (2010a) allows converting our CO luminosity measurements to total IR luminosities of $(2.3 \pm 0.5) \times 10^{12}\,L_\odot$ for HZ10 and $< 2.7 \times 10^{11}\,L_\odot$ for LBG-1, respectively, which are compatible with our FIR luminosity estimates. The best fit relation for starburst galaxies by Carilli & Walter (2013) would, on the other hand, over-predict the IR luminosity in HZ10 ($(3.9 \pm 0.8) \times 10^{12}\,L_\odot$) relative to our independent estimates. Adopting our best estimate of the gas mass and the star formation rate in HZ10 (Table 2) yields a gas depletion timescale (the inverse of the star formation efficiency) of 960^{+1200}_{-470} Myr, which is significantly longer than what is commonly measured in starburst galaxies and is instead compatible with typical star-forming galaxies. HZ10 therefore appears to be very rich in molecular gas, and the efficiency of star formation appears compatible with what is commonly observed in lower redshift, disk-like, main-sequence galaxies (e.g., Leroy et al. 2013).

The IR luminosity constraints implied by the CO upper limit in LBG-1 when adopting the main-sequence and starburst relations are approximately equal. Although the derived IR luminosity constraint is compatible with our uncertain, independent estimate within 1σ, our best estimates for the IR luminosity of LBG-1 are at least a factor of 2 higher, further suggesting that the CO luminosity in LBG-1 may be lower than in lower redshift galaxies with comparable SFR (Figure 5). If we adopt our best estimates for the SFR in LBG-1 based on the inferred IR luminosity, we can derive estimates of the gas depletion timescale for the gas masses derived from the long-wavelength dust method ($\sim 500^{+500}_{-250}$ Myr) and from the dynamical mass constraints ($\sim 280^{+420}_{-180}$ Myr). Assuming $\alpha_{\rm CO} = 4.5$, the CO upper limit corresponds to an upper limit on the gas depletion timescale of $\lesssim 2.8$ Gyr with 3σ confidence (i.e., with 99.7% probability).

In a second step, we also use our estimates for the gas reservoir physical sizes derived from the [CII] line to compare the gas surface density to the star formation rate density probed by the dust continuum flux and size (Figure 5), probing the physical drivers of star formation more directly, i.e., the Kennicutt-Schmidt law (Kennicutt 1998; Leroy et al. 2008; Bigiel et al. 2008; Daddi et al. 2010a; Bigiel et al. 2011; Schruba et al. 2011; Kennicutt & Evans 2012; Leroy et al. 2013). Specifically, we include in this comparison both Main Sequence galaxies at $z \sim 1-3$ (Tacconi et al. 2013; Daddi et al. 2010a) and very intensely star forming sub-millimeter galaxies (SMGs, Bouché et al. 2007; Bothwell et al. 2010). In particular, we focus our comparison on CRLE and AzTEC-3, two hyper-luminous DSFGs at $z > 5$ which are located in proximity of HZ10 and LBG-1, respectively. Based on their global gas masses and SFR, the gas depletion timescales for CRLE and AzTEC-3 are $\sim 45-50$ Myr (Riechers et al. 2010b, 2014; Pavesi et al. 2018b), i.e., an order of magnitude shorter than we observe in HZ10 and LBG-1. Due to the extreme compactness of the star formation in AzTEC-3 and CRLE, the local depletion timescale characterizing the ratio of gas and SFR surface densities are as short as $\sim 10-30$ Myr, while our estimates for HZ10 and LBG-1 are ~ 1 Gyr and $\lesssim 300$ Myr, respectively (Figure 5). Therefore, the physical efficiency, in terms of surface densities, may potentially differ by up to two orders of magnitude already among these galaxies at $z > 5$. This comparison shows that, while AzTEC-3 and CRLE have high star formation efficiency, compatible with other high redshift starbursts, HZ10 (and to a smaller degree LBG-1) appear to exhibit the lower efficiencies, longer depletion times typically observed in Main Sequence disks. Although the depletion time measurement in HZ10 is incompatible with that in the starbursts (e.g., Silverman et al. 2015, 2018), the significant systematic uncertainty implies compatibility with both the efficiency in $z \sim 0$ disk galaxies (e.g., Leroy et al. 2013) but also the potentially higher efficiency suggested for Main Sequence galaxies by Tacconi et al. (2013); Genzel et al. (2015); Scoville et al. (2016, 2017); Tacconi et al. (2018).

3.3. *Results from the [NII] measurements*

We tentatively detect [NII] 205 μm emission toward LBG-1 (at $\sim 3.4\sigma$), and HZ9 (at $\sim 3.1\sigma$), we confidently detect it from HZ10 (at $\gtrsim 6\sigma$), and we provide a constraining upper limit for HZ4 (Figures 1 & 2). We confirm the tentative detection toward LBG-1 and the detection toward HZ10 previously reported by Pavesi et al. (2016) achieving a higher signal-to-noise ratio. We measure [NII] and [CII] line properties using aperture spectra consistently for the whole sample (Table 1, see footnote 1). The [NII] emission from HZ10 appears extended, although the extended structure only has low significance ($\sim 2-3\sigma$, Figure 1). In order to measure the [NII] emission size we fit a circular Gaussian model to the integrated [NII] line visibilities from HZ10, using CASA UVMODELFIT. The moderate signal-to-noise ratio of the [NII] detections in LBG-1 and HZ9 does not allow measuring the [NII] emission size. We measure a deconvolved [NII] spatial FWHM size of $1''.71 \pm 0''.25$ for HZ10, cor-

[5] Due to the large uncertainty in the gas mass estimate, the 3σ CO limit only implies a 3σ limit of $\alpha_{\rm CO} > 0.2$ when appropriately propagated through posterior sampling. See footnote 4

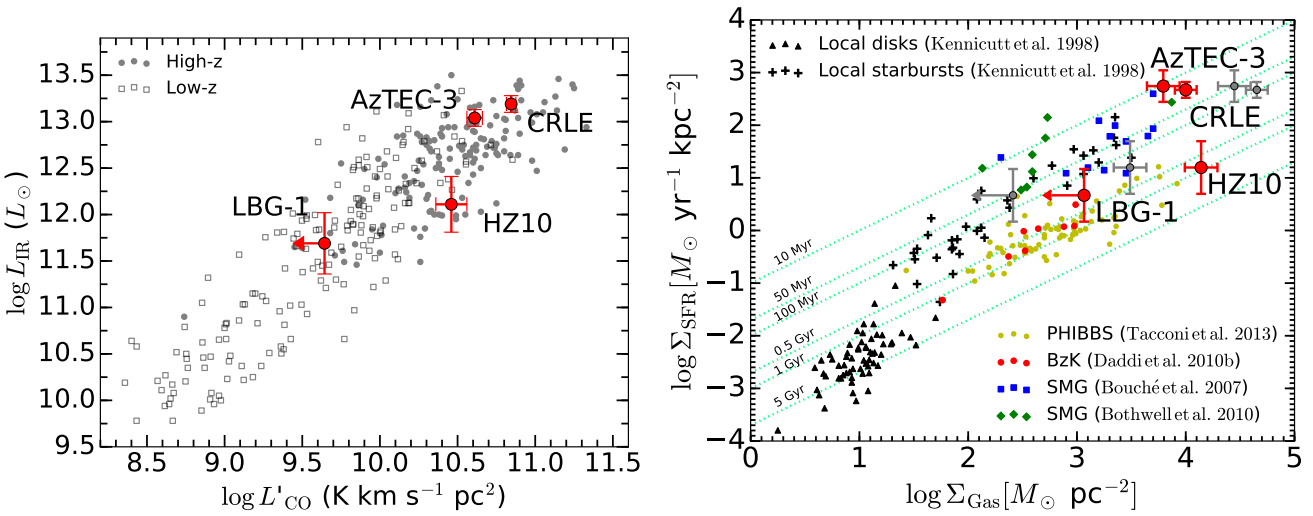

Figure 5. Left: IR luminosity observed in a sample of local and high redshift galaxies as a function of their CO luminosity, for comparison to the measurements in HZ10 and LBG-1 (Carilli & Walter 2013). We also include two $z > 5$ DSFGs for reference (AzTEC-3 and CRLE; Riechers et al. 2010b, 2014; Pavesi et al. 2018b,a), clearly occupying a distinct part of the parameter space. Right: Star formation rate surface density as a function of the gas mass surface density for a sample of local and high redshift galaxies, including HZ10, LBG-1, AzTEC-3 and CRLE (adapted from Daddi et al. 2010a, updated by Tacconi et al. 2013). The star formation rate surface density was estimated for the $z > 5$ galaxies through the FIR luminosity and the dust continuum sizes. The gas surface density was estimated for these galaxies through the CO luminosity and the [CII] emission spatial size. Following Daddi et al. (2010a) we adopt $\alpha_{CO} \sim 4.5$ for Main Sequence galaxies such as HZ10 and LBG-1 and the other disk galaxies, and $\alpha_{CO} = 0.8$ for starbursts such as CRLE, AzTEC-3, local starbursts and high-z sub-millimeter galaxies (SMGs). Fixed gas depletion time (corresponding to fixed star formation efficiency) lines are shown for characteristic time-scales spanning from 10 Myr to 5 Gyr (green lines).

responding to 10 ± 2 kpc. We use the same technique to measure an effective circular [CII] size of $0''.61 \pm 0''.04$, corresponding to 3.6 ± 0.2 kpc, which is compatible with our more sophisticated UV plane modeling (Appendix A). The [NII] line emission appears to be marginally more extended, than the [CII] emission, but higher resolution and higher signal to noise [NII] observations are necessary to confirm this finding. In particular, a manual inspection of the UV-radial profile of the [NII] line visibilities appears compatible with the size of the [CII] emission within the relative uncertainties.

We do not detect spatial offsets between the [NII] and [CII] line emission in LBG-1, HZ9 and HZ10. Although the [NII] line emission in HZ10 comes from the full [CII] velocity range, the comparison of the [NII] and [CII] spectra (Figure 2) suggests a possible differential intensity ratio, with stronger [NII] intensity coming from the red part of the emission (as previously found by Pavesi et al. 2016). The [NII] line velocity width appears narrower than [CII] toward LBG-1 and HZ9, although the limited signal-to-noise does not allow a precise measurement of the line width.

We here update our measurement of the [CII]/[NII] line ratio for HZ10 and LBG-1 (Pavesi et al. 2016), while expanding the sample to include HZ9 and HZ4 (Table 1, Figure 6). We confirm the relatively low line ratio for HZ10, compatible with most local and high redshift active star-forming galaxies (Pavesi et al. 2016). On the other hand, we also find a substantially higher ratio for HZ9, LBG-1 and HZ4, providing further evidence for the diversity of conditions at $z > 5$ already present in this small sample (Pavesi et al. 2016). The [CII]/[NII] line ratio is sensitive to the fraction of [CII] emission coming from ionized gas, rather than PDRs, because while [CII] may originate from both PDRs and ionized gas, [NII] is expected to only come from ionized gas due to its higher formation energy. The constant [CII]/[NII] line ratio in ionized gas (weakly dependent on density and radiation field) makes it a good tracer of the fraction of [CII] coming from ionized gas rather than PDRs (e.g., Oberst et al. 2006). We assume a line ratio of 3 ± 0.5 in the ionized gas (Díaz-Santos et al. 2017), to infer fractions of [CII] coming from PDRs of $83\% \pm 6\%$ for HZ10, $96\% \pm 2\%$ for HZ9, $93\% \pm 3\%$ for LBG-1 and $> 86\%$ for HZ4.

As previously described by Pavesi et al. (2016), a high [CII]/[NII] line ratio may be expected in the case of very high gas density, or of high intensity and hardness of the radiation field. The latter explanation appears consistent with observations of a high line ratio in local dwarf galaxies by Cormier et al. (2015), which may be interpreted as the consequence of high radiation intensity and hardness due to low metallicity conditions. A high intensity and hardness radiation field is expected to induce higher ionization conditions in the ionized gas. This implies weak [NII] and [CII] emission from ionized gas because nitrogen, carbon and oxygen are expected to be in a higher ionization state. This prediction is testable by observing strong [NIII] 57 μm and [OIII] 52 μm or 88 μm emission lines. Therefore, in analogy to the case of local dwarf galaxies, we interpret our high line ratio measurements and limits for HZ9, LBG-1 and HZ4 as indicative of low gas (and stellar) metallicity, relative to $z < 5$ galaxies of comparable masses ($\sim 10^{10}\,M_\odot$). On the other hand, the lower line ratio observed in HZ10 suggests higher metallicity in this galaxy, confirming the inference based on high dust and CO emission, and suggesting a particularly "mature, normal" galaxy at the same epoch (see also discussion by Faisst et al. 2017). We note that an alternative interpretation for the low [NII] luminosity may invoke lower nitrogen abundance, relative to carbon. While this abundance ratio change may also be a consequence of low metallicity conditions due to the secondary

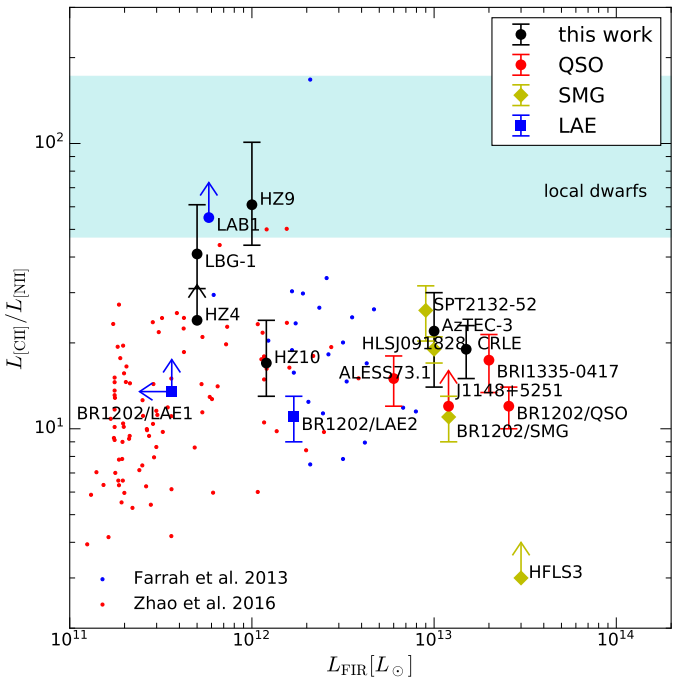

Figure 6. [CII]/[NII] line luminosity ratios observed in high redshift galaxies to-date as a function of their FIR luminosity (updated from Pavesi et al. 2016, with additions from Wagg et al. 2010; Umehata et al. 2017; Lu et al. 2018; Pavesi et al. 2018b). For comparison we also show a sample of local ULIRGs from Farrah et al. (2013) (using the [NII] 122 μm line) and LIRGs with [NII] (using the [NII] 205 μm line) from Zhao et al. (2016) and [CII] from Díaz-Santos et al. (2013). The range of ratios in dwarfs (Cormier et al. 2015) (using the [NII] 122 μm line) is shown as a cyan band. The [NII] 122 μm line measured in the indicated local samples was converted to a [NII] 205 μm luminosity assuming a ratio of 1/2.5, estimated by Herrera-Camus et al. (2016). The abscissa in the local samples are defined as total IR luminosity; no attempt was made to convert to a common FIR luminosity scale because it does not affect our interpretation.

nature of nitrogen, the carbon abundance dependence on gas phase metallicity is not well constrained.

4. DISCUSSION

The detection of bright CO emission from HZ10 represents the highest redshift CO detection from a "normal", Main Sequence galaxy to date (the next highest redshift CO line from a Main Sequence galaxy was serendipitously detected by Gowardhan et al. 2017 at $z \sim 3.2$). We note that HZ10 appears to have a very high gas fraction based on the measured CO luminosity ($M_{\rm gas} > M_{\rm stars}$ with high confidence and likely $M_{\rm gas} \sim 4-5 \times M_{\rm stars}$, Figure 4). Such high gas fractions may be expected at $z > 5$ based on the extrapolation of observed trends (e.g., Magdis et al. 2012; Genzel et al. 2015; Tacconi et al. 2018). A high gas fraction may also potentially be connected with the possibility of a galaxy merger in HZ10. Merging galaxies have been found to potentially show enhanced gas fractions (e.g., Pavesi et al. 2018a). Assuming $\alpha_{\rm CO} \sim 4.5$ for LBG-1 would imply a $\gtrsim 4$ times lower gas fraction, potentially suggesting significant scatter within the general population. However, the low CO luminosity in LBG-1 is likely to be due to low metallicity, as suggested by the faint [NII] emission (Pavesi et al. 2016), and the gas fraction may therefore be substantially higher.

Zavala et al. (2018) recently reported observations of CO and [CII] emission lines from the strongly lensed galaxy G09 83808 at $z \sim 6$, presenting analogies with HZ10. Although the inferred CO(1–0) luminosity of G09 83808 is approximately three times fainter than HZ10, the dust continuum emission is at least twice as bright (rest-frame 158 μm flux) indicating a significantly higher star formation efficiency than found in HZ10. Therefore, while G09 83808 appears to have a comparable star formation rate as HZ10 (within a factor of a few), its star formation resembles starbursts such as CRLE and AzTEC-3, while HZ10 is more gas rich and exhibits star forming conditions compatible with lower redshift Main Sequence, disk galaxies. This finding is in agreement with the ten times higher [CII]/FIR ratio in HZ10 relative to G09 83808. This ratio is a probe of the local physical density of star formation and is inversely proportional to the starburst intensity. Based on PDR models, a fixed PDR gas density implies that the far UV (FUV) field intensity (G_0) scales inversely with [CII]/FIR (to a power of $\sim 1-1.2$) (Wolfire et al. 1990; Kaufman et al. 1999; Stacey et al. 2010). This scaling implies that the FUV intensity in G09 83808 may be $\sim 10-15$ times higher than in HZ10, confirming that HZ10 may be forming stars in a much less intense environment.

The finding of significant dust and, especially, CO emission from HZ10 suggests that a fraction of "normal" galaxies (not extreme starbursts) at $z > 5$ may be rich in molecular gas and significantly metal-enriched, in contrast to some previous indications (e.g., Tan et al. 2013, 2014). This finding is in agreement with the recent measurement of a high volume density of CO-selected galaxies at $z > 5$ by the CO Luminosity Density at High-z (COLDz) project (Pavesi et al. 2018a; Riechers et al. 2018). Although the galaxies selected by COLDz at $z > 5$ are bright starbursts, their volume density is significantly higher than predicted by current models (Riechers et al. 2018). However, if HZ10 had been located within the COLDz field of view it would have been selected by the blind line search based on the survey detection limit (Pavesi et al. 2018a), therefore placing an upper limit to the volume density of evolved, gas-rich "normal" galaxies at $z > 5$ with CO luminosity greater than HZ10 of $\lesssim 5 \times 10^{-5}\,{\rm Mpc}^{-3}$ (Riechers et al. 2018).

HZ10 is believed to reside in a galaxy overdensity at $z \sim 5.7$, potentially indicating a protocluster environment (Pavesi et al. 2018b). In particular, the presence of the bright hyper-starburst CRLE only ~ 70 kpc away constitutes evidence for a possible physical association. This association with the massive, dusty galaxy CRLE and the protocluster may be related to the advanced evolutionary stage of HZ10. If this connection were confirmed, it would point to a more rapid evolution for galaxies in higher density environments (e.g., Chiang et al. 2017).

The PHIBBS survey has measured star formation efficiency and gas fractions for lower redshift (up to $z \sim 2-3$) Main Sequence galaxies (Tacconi et al. 2013; Genzel et al. 2015; Tacconi et al. 2018). Based on the extrapolation of the latest measured trends reported by Tacconi et al. (2018), combining the PHIBBS CO measurements with the dust-based estimates by Scoville et al. (2016, 2017) we can derive expectations for the average gas fraction and depletion times expected for Main Se-

quence galaxies such as HZ10 at $z \sim 5.7$. We derive an approximate gas depletion timescale of ~ 400 Myr, which is compatible with our estimate for HZ10 within 1σ (in particular due to the uncertainty in the estimate of total IR luminosity). The molecular gas fraction predicted by the fitting formula suggested by Tacconi et al. (2018) is $M_{\rm gas} \sim M_{\rm stars}$ (the quadratic fitting formula predicts, perhaps artificially, a turnover of the trend at $z \sim 3.5$), which is lower than observed in HZ10. Our observations therefore suggest that the increase in molecular gas fraction with redshift may continue beyond $z \sim 3$, although with very limited statistical power due to the small sample size. In summary, HZ10 shows the characteristic properties of lower redshift Main Sequence galaxies, all the way back to the first billion years of cosmic time.

Vallini et al. (2018) presented some of the latest models of the CO line emission from "normal" galaxies at $z > 5$. They modeled the radiative transfer affecting CO emission from a clumpy molecular medium in a $M_{\rm stars} \sim 10^{10}\,M_\odot$ Main Sequence galaxy at $z \sim 6$. Although their model galaxy is characterized by sub-solar ($0.5Z_\odot$) metallicity they predict a low effective CO conversion factor of $\alpha_{\rm CO} \sim 1.5$ due to the dominant effect of warmer gas, high turbulence and high gas surface density (Vallini et al. 2018). While this low $\alpha_{\rm CO}$ may be allowed for HZ10 (although disfavored by our dynamical mass estimates), it is ruled out for the more typical LBG-1 if the gas mass is predominantly molecular. In addition, the predicted CO luminosity for the "typical" model galaxy is ~ 20 times lower than observed in HZ10, suggesting that the molecular gas mass may be significantly underestimated. Therefore, HZ10 may be more mature and may therefore not be analogous to the model galaxy, but rather to the lower redshift Main Sequence galaxies observed at $z \sim 2-3$. Although our constraints for the CO luminosity in LBG-1 are compatible with the model prediction, the higher dynamical mass estimates suggest higher gas masses for LBG-1 than the molecular mass predicted by the models. A possible interpretation of this result may invoke a significant fraction of gas in the atomic phase, which may dominate the total gas mass in such "typical", massive galaxies. Based on the [CII] luminosity in LBG-1 we can derive an estimate of the atomic PDR mass of $\sim 2-5\times10^9\,M_\odot$ following Stacey et al. (1991), which may be comparable to the molecular gas mass for low $\alpha_{\rm CO}$, but it is unlikely to provide the total gas mass inferred from our dynamical mass estimate.

The measurement of [CII] and dust continuum emission from the first sample of "normal", rest-UV selected galaxies revealed a variety of star-forming conditions (Capak et al. 2015). The finding of bright CO line emission from HZ10 and faint emission from LBG-1 is in agreement with the interpretation of a range of metallicities and dust-to-gas ratios being the main contributors to the variation within the sample (Capak et al. 2015). This interpretation is strongly supported by the significant difference in [CII]/[NII] ratio between HZ10 and LBG-1 already noted by Pavesi et al. (2016). Faint [NII] emission relative to [CII] directly implies (with the possible caveat of differences in the C/N abundance ratio) low contribution of the ionized gas to the [CII] emission, which may therefore be predominantly due to emission from neutral PDRs. The simplest interpretation for faint [NII] emission suggests higher ionization conditions in the ionized gas, predicting bright [NIII] and [OIII] emission, instead. This interpretation would suggest that intensity and, especially, hardness of the radiation field may be the most relevant physical parameter affecting this line ratio. Recent detections of bright [OIII] 88 μm line emission at high redshift support this interpretation and suggest that [OIII] may be even brighter than [CII] in "normal" galaxies at very high redshift (e.g., Inoue et al. 2016; Laporte et al. 2017; Carniani et al. 2017; Marrone et al. 2018; Hashimoto et al. 2018b,c,a; Tamura et al. 2018), as typically observed in local dwarfs (Cormier et al. 2015). Furthermore, recent optical studies of LBGs and LAEs have also found increasing [OIII]λ5008 brightness at high redshift together with high sSFR and low metallicity (e.g., Strom et al. 2017a,b). The metallicity dependence may also be responsible for the downturn due to reduced oxygen abundance at even lower metallicity (Harikane et al. 2018).

Faisst et al. (2017) explore the level of maturity, stellar population properties and dust attenuation in $z = 5-6$ "normal" galaxies through the IRX/$\beta_{\rm UV}$ diagnostic plane. While IRX, defined as the ratio $L_{\rm IR}/L_{\rm UV}$, represents the prevalence of dust-obscured star-formation, $\beta_{\rm UV}$ is the power-law slope of the UV emission, which bears the imprint of dust reddening. A correlation between these quantities was observed to hold for local starburst galaxies, and approximately holding up to high redshift (e.g., Meurer et al. 1999; Reddy et al. 2006, 2010, 2018; Bouwens et al. 2016), however variations may be expected due to varying dust properties, star-formation geometry and stellar population ages (e.g., Faisst et al. 2017; Narayanan et al. 2018). These diagnostics suggest that HZ10 may resemble dusty star-forming galaxies, with elevated IR to UV luminosity ratio, intriguingly sharing similarities to lower redshift IR-selected galaxies (e.g., Casey et al. 2014). However, HZ10 was selected through the LBG and LAE techniques at $z \sim 5.7$ and appears "typical" based on its UV emission. In particular, HZ10 lies within the scatter of the Main Sequence at this redshift (e.g., Speagle et al. 2014; Capak et al. 2015; Barišić et al. 2017; Faisst et al. 2017). Faisst et al. (2017) also interpret the observed properties of LBG-1 as being consistent with lower dust and metal abundances, likely connected to young stellar populations. The IRX/$\beta_{\rm UV}$ diagnostic, however, would suggest that HZ4, and especially HZ9, may be more dusty than LBG-1 since they lie on or above the local Meurer et al. (1999) relation (Faisst et al. 2017). However, the measured [CII]/[NII] ratios for HZ4 and HZ9 are compatible with that in LBG-1 and significantly higher than the ratio in HZ10 (Figure 6). The intriguing observation of faint [NII] emission together with relatively bright dust continuum in HZ9 therefore suggests the presence of additional variables controlling the relationship between the level of dust obscuration and the metallicity (or age of the most recent stellar population) which may be critical to diagnose the interplay between gas inflows, outflows and star formation. An important next step would require measuring the CO line luminosity from HZ9 as well as achieving a detection in LBG-1. In case of relatively bright CO emission (e.g., in relation to its FIR luminosity) from HZ9, the high [CII]/[NII] line ratio would not be explained by the analogy to local dwarf galaxies and would point

to unexplored star formation conditions. However, faint CO line emission from HZ9 would either suggest variations in the dust SED shape or would intriguingly suggest the possibility of significant dust-obscured star formation even in more "typical", lower metallicity, younger high redshift galaxies. The ratio of our continuum measurements tentatively suggests higher dust temperatures in HZ9 than in HZ10. If correct, this might imply that the moderate IR luminosity in HZ9 may be due to higher temperatures, perhaps associated with higher radiation intensity, rather than a high dust content (Faisst et al. 2017). Ferrara et al. (2017) suggested that galaxies at $z > 5$ may be FIR-faint due to colder dust than "normal" due to the very high molecular gas fraction. Their prediction of bright CO emission, specifically from galaxies with low IRX, may be in conflict with our deep upper limits on the CO luminosity from LBG-1. However, this effect may link the high molecular gas mass fraction in HZ10 to the tentatively lower dust temperature we observe in this galaxy relative to the rest of the sample (Ferrara et al. 2017).

The faint [NII] emission from HZ4 and HZ9, together with significant dust-obscured star formation, may be analogous to the properties observed in the eastern component of SPT0311-58 (Marrone et al. 2018). This galaxy at $z = 6.90$ was shown to display high [OIII] 88μm luminosity ($\sim 2\times$ its [CII] luminosity) while being characterized by very high dust-obscured star formation (at the level observed in HZ9 and HZ10). Similarly, the bright [OIII] emitters studied by Hashimoto et al. (2018b) and Tamura et al. (2018) at $z > 7$ which also show significant dust emission may be somewhat analogous to the case we observe in HZ9, i.e., high intensity and hardness of the radiation causing a higher ionization state in the ionized ISM while showing significant dust-obscured star formation. Furthermore, a comparison of the [OIII]/[CII] luminosity in two quasars at $z \sim 6$ suggests that this line ratio may strongly correlate with dust temperatures (Hashimoto et al. 2018a), supporting our interpretation of higher dust temperatures in [NII]-faint galaxies. We therefore suggest that a higher dust temperature may drive the observed FIR luminosity in such galaxies, perhaps due to a significant contribution from dust in the ionized regions (Faisst et al. 2017).

In order to assess how common the different star forming conditions observed in LBG-1, HZ9 and HZ10 are, larger samples of "normal" galaxies at $z = 5 - 6$ need to be studied. The ALMA Large Program to Investigate [CII] at Early Times (ALPINE)[6], is now observing the [CII] and dust emission from large samples of typical galaxies at $4 < z < 6$ over a wide range of stellar mass and star formation rate. While the brightness of [CII] and dust continuum, and their relation to the ultra-violet flux, provide a wealth of information (e.g., distinguishing LBG-1 from HZ10-type conditions), our analysis shows that relevant residual degrees of freedom are unconstrained unless either CO or a tracer of the ionized gas (such as [NII], [NIII] or [OIII]) is measured in addition to [CII] (to distinguish HZ10 from HZ9-type conditions) possibly due to metallicity, and/or dust temperature variations. Furthermore, resolved observations for larger samples of galaxies are necessary because accurate dynamical masses may be the best way to constrain the gas mass and, hence, to directly infer the $\alpha_{\rm CO}$ conversion factor.

[6] https://cesam.lam.fr/a2c2s/index.php

5. CONCLUSIONS

We have presented measurements of CO(2–1) line emission from two "normal" Lyman Break Galaxies galaxies, at the end of the "Epoch of Reionization", achieving the highest redshift low-J CO detection from a Main Sequence galaxy to date. We have found large variation in the CO line luminosity between the two targeted sources which may not be completely accounted for by SFR variation (the CO luminosity ratio is $\gtrsim$6.5 while the SFR ratio is ~ 3). While this difference in CO luminosity may suggest variations in star formation efficiency, it appears consistent with our expectation of lower gas metallicity and dust abundance strongly affecting the CO abundance. We infer a large molecular gas reservoir in at least one of the sources, suggesting low efficiency star formation with gas depletion time $\sim$1 Gyr already at $z \sim 6$, analogous to what is commonly observed in lower redshift disk galaxies. This low efficiency contrasts to what is typically observed in $z > 5$ starbursts and provides the first evidence of such "Main sequence" star-forming conditions at $z > 3$. We also find evidence for a continuously rising gas fraction up to $z \sim 6$, although our sample may suggest either significant scatter or systematic variations in the $\alpha_{\rm CO}$ conversion factor.

By observing the largest sample of "normal" galaxies at $z > 5$ in [NII] 205 μm emission to date, we find a general trend of increasing [CII]/[NII] ratios with lower IR luminosity; consistent with what was previously reported by Pavesi et al. (2016). Our findings support an interpretation where low gas and stellar metallicity raise the ionization state of carbon and nitrogen in the ionized gas. This interpretation suggest that the large majority of [CII] emission from most "normal" galaxies at $z > 5$ may emerge from the neutral gas phase. We also find a high [CII]/[NII] ratio in our sample with moderate IR luminosity, suggesting either significant dust temperature variations affecting the IR luminosity estimate, or the possibility of a young starburst with high radiation intensity and hardness (and potentially low metallicity) together with substantial dust obscuration. Our findings imply that a significant fraction of Main Sequence star formation taking place up to $z \sim 6$ may resemble the conditions observed in "normal" galaxies at lower redshift, suggesting that the efficiency of star formation may only weakly depend on those physical properties which are affected by redshift evolution. In particular, the high inferred gas fractions and the higher merger rates do not appear to significantly affect Main Sequence star formation. Although low metallicity may be common in the Main Sequence galaxy population at $z > 5$, we do not find conclusive evidence for an effect on the star forming conditions, although larger samples and more sensitive observations are needed to study this fainter population.

Acknowledgments We thank Chelsea Sharon and Avani Gowardhan for useful discussion. R.P. and D.R. acknowledge support from the National Science Foundation under grant number AST-1614213 to Cornell University. R.P. acknowledges support through award SOSPA3-008 from the NRAO. The National Radio Astronomy Observatory is a facil-

ity of the National Science Foundation operated under cooperative agreement by Associated Universities, Inc. This paper makes use of the following ALMA data: ADS/JAO.ALMA#2015.1.00928.S, 2015.1.00388.S, 2012.1.00523.S, 2011.0.00064.S. ALMA is a partnership of ESO (representing its member states), NSF (USA) and NINS (Japan), together with NRC (Canada), NSC and ASIAA (Taiwan), and KASI (Republic of Korea), in cooperation with the Republic of Chile. The Joint ALMA Observatory is operated by ESO, AUI/NRAO and NAOJ.

APPENDIX

A. DYNAMICAL MODELING

We carry out dynamical modeling of the [CII] line emission from HZ10 and HZ9 using a rotating disk model generated by `KinMS` (Davis et al. 2013), fitted to the visibility data using `GALARIO` Tazzari et al. (2018) and `Multinest` (Feroz et al. 2009), using the method[7] previously described by Pavesi et al. (2018b). We model the continuum as two and one Gaussian components for HZ10 and HZ9, respectively. We model the line emission intensity as a Gaussian profile and the rotation curve as a "tangent" function parametrised by the maximum velocity and the half-maximum radius (Table 3). We fit a total of 18 parameters for HZ10 (also including line flux, disk center along each coordinate and continuum sizes, fluxes and position for both components) and 12 parameters for HZ9 (also including line flux, disk center along each coordinate and continuum size and flux) as afforded by the available signal-to-noise ratio. The data, median parameter model (indistinguishable from the best-fit model) and residuals are shown in Figures 7 and 8, together with the derived probabilistic constraints to the rotation curves and the implied dynamical masses.

Table 3
Results of dynamical modeling for our sample galaxies.

Parameter (Units)	HZ10 16th perc.	HZ10 50th perc.	HZ10 84th perc.	HZ9 16th perc.	HZ9 50th perc.	HZ9 84th perc.
Gas dispersion (km s^{-1})	210	218	226	80	89	100
Emission FWHM (arcsec)	0.84	0.88	0.91	0.47	0.51	0.55
Maximum velocity (km s^{-1})	380	430	510	300	445	750
Velocity scale length (arcsec)	0.12	0.18	0.28	0.014	0.03	0.08
Inclination (degrees)	59	61	63	13	21	31
Position angle (degrees)	−7	−5	−3	71	77	83

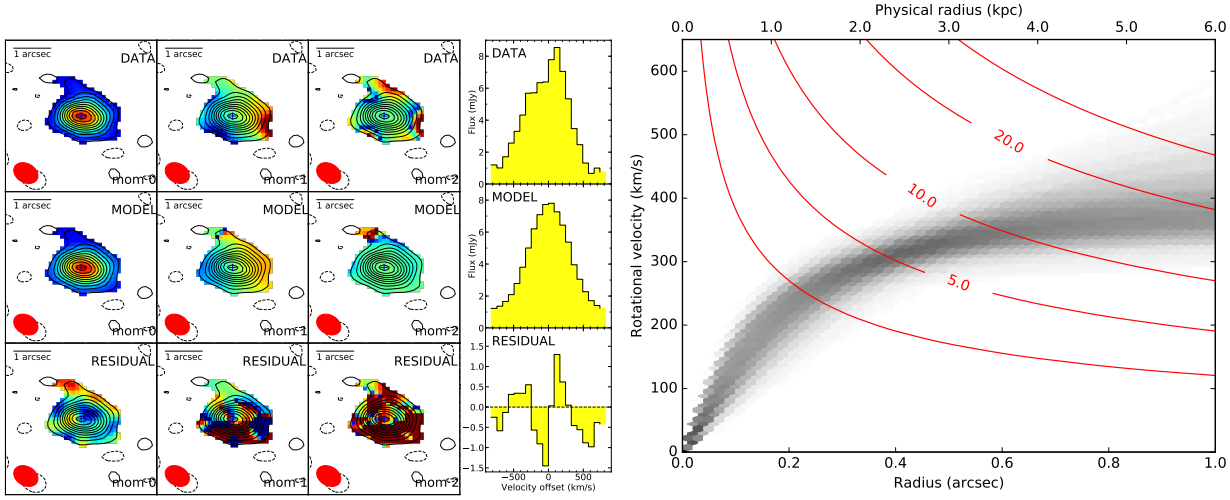

Figure 7. Left: Visibility space dynamical modeling results for the [CII] line emission in HZ10. We show the "natural" weighting line moment 0 (intensity), 1 (velocity) and 2 (dispersion) maps and spectra for the data, the single-disk model corresponding to posterior median parameters, and the visibility residuals. Two-Gaussian components were adopted as model for the continuum. Right: Probabilistic constraints to the rotation curve for a "tan" model with two disk modeling parameters (maximum velocity and half-velocity radius). The darker shading corresponds to higher probability density, as determined by the MCMC samples. We also show the enclosed dynamical mass in units of $10^{10}\,M_\odot$ (red curves).

[7] Python code available at https://github.com/pavesiriccardo/UVmodeldisk

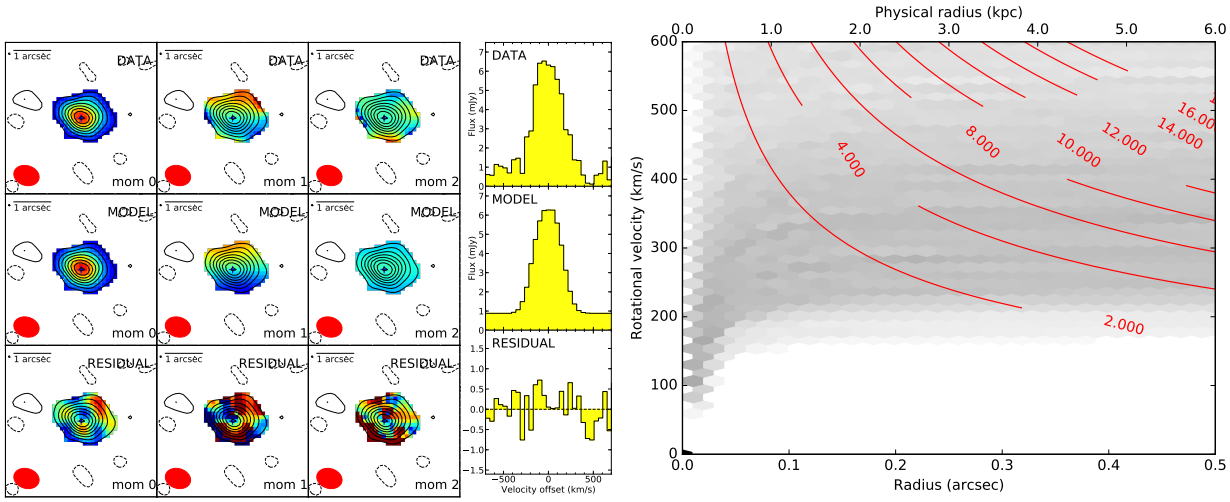

Figure 8. Dynamical modeling results for HZ9. A single Gaussian component was adopted as continuum model. See Figure 7 for further details.

REFERENCES

Barišić, I., Faisst, A. L., Capak, P. L., et al. 2017, ApJ, 845, 41
Behroozi, P., Wechsler, R., Hearin, A., & Conroy, C. 2018, ArXiv e-prints, arXiv:1806.07893
Bigiel, F., Leroy, A., Walter, F., et al. 2008, AJ, 136, 2846
Bigiel, F., Leroy, A. K., Walter, F., et al. 2011, ApJ, 730, L13
Bolatto, A. D., Wolfire, M., & Leroy, A. K. 2013, ARA&A, 51, 207
Bothwell, M. S., Chapman, S. C., Tacconi, L., et al. 2010, MNRAS, 405, 219
Bouché, N., Cresci, G., Davies, R., et al. 2007, ApJ, 671, 303
Bournaud, F., Daddi, E., Weiß, A., et al. 2015, A&A, 575, A56
Bournaud, F., Perret, V., Renaud, F., et al. 2014, ApJ, 780, 57
Bourne, N., Dunne, L., Bendo, G. J., et al. 2013, MNRAS, 436, 479
Bouwens, R. J., Illingworth, G. D., Oesch, P. A., et al. 2015, ApJ, 803, 34
Bouwens, R. J., Aravena, M., Decarli, R., et al. 2016, ApJ, 833, 72
Buckley, M. R., & Peter, A. H. G. 2017, ArXiv e-prints, arXiv:1712.06615
Capak, P. L., Carilli, C., Jones, G., et al. 2015, Nature, 522, 455
Carilli, C. L., & Walter, F. 2013, ARA&A, 51, 105
Carniani, S., Maiolino, R., Pallottini, A., et al. 2017, A&A, 605, A42
Casey, C. M., Scoville, N. Z., Sanders, D. B., et al. 2014, ApJ, 796, 95
Castellano, M., Pentericci, L., Vanzella, E., et al. 2018, ApJ, 863, L3
Chiang, Y.-K., Overzier, R. A., Gebhardt, K., & Henriques, B. 2017, ApJ, 844, L23
Coppin, K. E. K., Swinbank, A. M., Neri, R., et al. 2007, ApJ, 665, 936
Cormier, D., Madden, S. C., Lebouteiller, V., et al. 2014, A&A, 564, A121
—. 2015, A&A, 578, A53
da Cunha, E., Groves, B., Walter, F., et al. 2013, ApJ, 766, 13
Daddi, E., Elbaz, D., Walter, F., et al. 2010a, ApJ, 714, L118
Daddi, E., Bournaud, F., Walter, F., et al. 2010b, ApJ, 713, 686
Daddi, E., Dannerbauer, H., Liu, D., et al. 2015, A&A, 577, A46
Davé, R., Finlator, K., & Oppenheimer, B. D. 2011, MNRAS, 416, 1354
—. 2012, MNRAS, 421, 98
Davis, T. A., Alatalo, K., Bureau, M., et al. 2013, MNRAS, 429, 534
Decarli, R., Walter, F., Carilli, C., et al. 2014, ApJ, 782, L17
Dessauges-Zavadsky, M., Zamojski, M., Schaerer, D., et al. 2015, A&A, 577, A50
Dessauges-Zavadsky, M., Zamojski, M., Rujopakarn, W., et al. 2017, A&A, 605, A81
Díaz-Santos, T., Armus, L., Charmandaris, V., et al. 2013, ApJ, 774, 68
—. 2017, ApJ, 846, 32
Eales, S., Smith, M. W. L., Auld, R., et al. 2012, ApJ, 761, 168
Faisst, A. L., Capak, P., Hsieh, B. C., et al. 2016, ApJ, 821, 122
Faisst, A. L., Capak, P. L., Yan, L., et al. 2017, ApJ, 847, 21
Farrah, D., Lebouteiller, V., Spoon, H. W. W., et al. 2013, ApJ, 776, 38
Feroz, F., Hobson, M. P., & Bridges, M. 2009, MNRAS, 398, 1601
Ferrara, A. 2016, in Understanding the Epoch of Cosmic Reionization: Challenges and Progress, ed. A. Mesinger, Vol. 423, 163
Ferrara, A., Hirashita, H., Ouchi, M., & Fujimoto, S. 2017, MNRAS, 471, 5018
Geach, J. E., Smail, I., Moran, S. M., et al. 2011, ApJ, 730, L19
Genzel, R., Tacconi, L. J., Lutz, D., et al. 2015, ApJ, 800, 20
Gowardhan, A., Riechers, D. A., Daddi, E., et al. 2017, ApJ, 838, 136
Groves, B. A., Schinnerer, E., Leroy, A., et al. 2015, ApJ, 799, 96
Gullberg, B., De Breuck, C., Vieira, J. D., et al. 2015, MNRAS, 449, 2883
Harikane, Y., Ouchi, M., Shibuya, T., et al. 2018, ApJ, 859, 84
Hashimoto, T., Inoue, A. K., Tamura, Y., et al. 2018a, ArXiv e-prints, arXiv:1811.00030
Hashimoto, T., Inoue, A. K., Mawatari, K., et al. 2018b, ArXiv e-prints, arXiv:1806.00486
Hashimoto, T., Laporte, N., Mawatari, K., et al. 2018c, Nature, 557, 392
Herrera-Camus, R., Bolatto, A., Smith, J. D., et al. 2016, ApJ, 826, 175
Hildebrand, R. H. 1983, Quarterly Journal of the Royal Astronomical Society, 24, 267
Hollenbach, D. J., & Tielens, A. G. G. M. 1997, Annual Review of Astronomy and Astrophysics, 35, 179
Hopkins, P. F., Kereš, D., Oñorbe, J., et al. 2014, MNRAS, 445, 581
Inoue, A. K., Tamura, Y., Matsuo, H., et al. 2016, Science, 352, 1559
Jameson, K. E., Bolatto, A. D., Wolfire, M., et al. 2018, ApJ, 853, 111
Jones, G. C., Carilli, C. L., Shao, Y., et al. 2017, ApJ, 850, 180
Kaufman, M. J., Wolfire, M. G., Hollenbach, D. J., & Luhman, M. L. 1999, ApJ, 527, 795
Kennicutt, R. C., & Evans, N. J. 2012, ARA&A, 50, 531
Kennicutt, Jr., R. C. 1998, ApJ, 498, 541
Krumholz, M. R., Burkhart, B., Forbes, J. C., & Crocker, R. M. 2018, MNRAS, 477, 2716
Laporte, N., Ellis, R. S., Boone, F., et al. 2017, ApJ, 837, L21
Leroy, A. K., Walter, F., Brinks, E., et al. 2008, AJ, 136, 2782
Leroy, A. K., Walter, F., Bigiel, F., et al. 2009, AJ, 137, 4670
Leroy, A. K., Bolatto, A., Gordon, K., et al. 2011, ApJ, 737, 12
Leroy, A. K., Walter, F., Sandstrom, K., et al. 2013, AJ, 146, 19
Lilly, S. J., Carollo, C. M., Pipino, A., Renzini, A., & Peng, Y. 2013, ApJ, 772, 119
Lu, N., Cao, T., Díaz-Santos, T., et al. 2018, ApJ, 864, 38
Luhman, M. L., Satyapal, S., Fischer, J., et al. 1998, ApJ, 504, L11
Ma, X., Hopkins, P. F., Garrison-Kimmel, S., et al. 2018, MNRAS, 478, 1694
Madden, S. C., Poglitsch, A., Geis, N., Stacey, G. J., & Townes, C. H. 1997, ApJ, 483, 200
Magdis, G. E., Daddi, E., Elbaz, D., et al. 2011, ApJ, 740, L15
Magdis, G. E., Daddi, E., Béthermin, M., et al. 2012, ApJ, 760, 6
Magnelli, B., Saintonge, A., Lutz, D., et al. 2012, A&A, 548, A22
Maiolino, R., Caselli, P., Nagao, T., et al. 2009, A&A, 500, L1
Maiolino, R., Cox, P., Caselli, P., et al. 2005, A&A, 440, L51
Malhotra, S., Kaufman, M. J., Hollenbach, D., et al. 2001, ApJ, 561, 766
Maloney, P., & Black, J. H. 1988, ApJ, 325, 389
Marrone, D. P., Spilker, J. S., Hayward, C. C., et al. 2018, Nature, 553, 51
Masters, D., Faisst, A., & Capak, P. 2016, ApJ, 828, 18
Meurer, G. R., Heckman, T. M., & Calzetti, D. 1999, ApJ, 521, 64
Moster, B. P., Naab, T., & White, S. D. M. 2018, MNRAS, 477, 1822
Nagao, T., Maiolino, R., De Breuck, C., et al. 2012, A&A, 542, L34
Nagao, T., Maiolino, R., Marconi, A., & Matsuhara, H. 2011, A&A, 526, A149
Narayanan, D., Davé, R., Johnson, B. D., et al. 2018, MNRAS, 474, 1718
Oberst, T. E., Parshley, S. C., Stacey, G. J., et al. 2006, ApJ, 652, L125
Orr, M. E., Hayward, C. C., Hopkins, P. F., et al. 2018, MNRAS, 478, 3653
Pavesi, R., Riechers, D. A., Capak, P. L., et al. 2016, ApJ, 832, 151
Pavesi, R., Sharon, C. E., Riechers, D. A., et al. 2018a, ApJ, 864, 49
Pavesi, R., Riechers, D. A., Sharon, C. E., et al. 2018b, ApJ, 861, 43
Reddy, N. A., Erb, D. K., Pettini, M., Steidel, C. C., & Shapley, A. E. 2010, ApJ, 712, 1070
Reddy, N. A., Steidel, C. C., Fadda, D., et al. 2006, ApJ, 644, 792
Reddy, N. A., Oesch, P. A., Bouwens, R. J., et al. 2018, ApJ, 853, 56
Riechers, D. A., Carilli, C. L., Walter, F., & Momjian, E. 2010a, ApJ, 724, L153
Riechers, D. A., Capak, P. L., Carilli, C. L., et al. 2010b, ApJ, 720, L131
Riechers, D. A., Bradford, C. M., Clements, D. L., et al. 2013, Nature, 496, 329

Riechers, D. A., Carilli, C. L., Capak, P. L., et al. 2014, ApJ, 796, 84
Riechers, D. A., Pavesi, R., Sharon, C. E., et al. 2018, ArXiv e-prints, arXiv:1808.04371
Sandstrom, K. M., Leroy, A. K., Walter, F., et al. 2013, ApJ, 777, 5
Schruba, A., Leroy, A. K., Walter, F., et al. 2011, AJ, 142, 37
Scoville, N., Arnouts, S., Aussel, H., et al. 2013, ApJS, 206, 3
Scoville, N., Sheth, K., Aussel, H., et al. 2016, ApJ, 820, 83
Scoville, N., Lee, N., Vanden Bout, P., et al. 2017, ApJ, 837, 150
Scoville, N. Z. 2013, Evolution of star formation and gas, ed. J. Falcón-Barroso & J. H. Knapen, 491
Sharda, P., Federrath, C., da Cunha, E., Swinbank, A. M., & Dye, S. 2018, MNRAS, 477, 4380
Silverman, J. D., Daddi, E., Rodighiero, G., et al. 2015, ApJ, 812, L23
Silverman, J. D., Rujopakarn, W., Daddi, E., et al. 2018, ApJ, 867, 92
Smith, J. D. T., Croxall, K., Draine, B., et al. 2017, ApJ, 834, 5
Speagle, J. S., Steinhardt, C. L., Capak, P. L., & Silverman, J. D. 2014, ApJS, 214, 15
Stacey, G. J., Geis, N., Genzel, R., et al. 1991, ApJ, 373, 423
Stacey, G. J., Hailey-Dunsheath, S., Ferkinhoff, C., et al. 2010, ApJ, 724, 957
Strandet, M. L., Weiss, A., De Breuck, C., et al. 2017, ApJ, 842, L15
Strom, A. L., Steidel, C. C., Rudie, G. C., Trainor, R. F., & Pettini, M. 2017a, ArXiv e-prints, arXiv:1711.08820
Strom, A. L., Steidel, C. C., Rudie, G. C., et al. 2017b, ApJ, 836, 164
Tacchella, S., Bose, S., Conroy, C., Eisenstein, D. J., & Johnson, B. D. 2018, ArXiv e-prints, arXiv:1806.03299
Tacconi, L. J., Neri, R., Genzel, R., et al. 2013, ApJ, 768, 74
Tacconi, L. J., Genzel, R., Saintonge, A., et al. 2018, ApJ, 853, 179
Tamura, Y., Mawatari, K., Hashimoto, T., et al. 2018, ArXiv e-prints, arXiv:1806.04132
Tan, Q., Daddi, E., Sargent, M., et al. 2013, ApJ, 776, L24
Tan, Q., Daddi, E., Magdis, G., et al. 2014, A&A, 569, A98
Tazzari, M., Beaujean, F., & Testi, L. 2018, MNRAS, 476, 4527
Tremonti, C. A., Heckman, T. M., Kauffmann, G., et al. 2004, ApJ, 613, 898
Umehata, H., Matsuda, Y., Tamura, Y., et al. 2017, ApJ, 834, L16
Vallini, L., Pallottini, A., Ferrara, A., et al. 2018, MNRAS, 473, 271
Vincenzo, F., Belfiore, F., Maiolino, R., Matteucci, F., & Ventura, P. 2016, MNRAS, 458, 3466
Wagg, J., Carilli, C. L., Wilner, D. J., et al. 2010, A&A, 519, L1
Walter, F., Riechers, D., Cox, P., et al. 2009, Nature, 457, 699
Walter, F., Decarli, R., Carilli, C., et al. 2012, Nature, 486, 233
Wolfire, M. G., Hollenbach, D., & Tielens, A. G. G. M. 1989, ApJ, 344, 770
Wolfire, M. G., Tielens, A. G. G. M., & Hollenbach, D. 1990, ApJ, 358, 116
Zavala, J. A., Montaña, A., Hughes, D. H., et al. 2018, Nature Astronomy, 2, 56
Zhao, Y., Lu, N., Xu, C. K., et al. 2016, ApJ, 819, 69